

Self-organization of mortal filaments and its role in bacterial division ring formation

Received: 5 May 2023

Accepted: 27 June 2024

Published online: 12 August 2024

 Check for updates

Christian Vanhille-Campos ^{1,2}, Kevin D. Whitley ³, Philipp Radler ^{1,4},
Martin Loose ¹, Séamus Holden ⁵ & Andela Šarić ¹ ✉

Filaments in the cell commonly treadmill. Driven by energy consumption, they grow on one end while shrinking on the other, causing filaments to appear motile even though individual proteins remain static. This process is characteristic of cytoskeletal filaments and leads to collective filament self-organization. Here we show that treadmilling drives filament nematic ordering by dissolving misaligned filaments. Taking the bacterial FtsZ protein involved in cell division as an example, we show that this mechanism aligns FtsZ filaments *in vitro* and drives the organization of the division ring in living *Bacillus subtilis* cells. We find that ordering via local dissolution also allows the system to quickly respond to chemical and geometrical biases in the cell, enabling us to quantitatively explain the ring formation dynamics *in vivo*. Beyond FtsZ and other cytoskeletal filaments, our study identifies a mechanism for self-organization via constant birth and death of energy-consuming filaments.

Cytoskeletal filaments are active cellular elements that continuously grow and shrink through addition and removal of subunits. One prominent example of this activity is treadmilling—a process by which protein filaments grow on one end while the other end shrinks at an equal rate. This dynamic behaviour is driven by nucleotide hydrolysis and results in the filaments seemingly moving, despite the individual filament monomers remaining in one place¹. Many essential cytoskeletal filaments, such as actin, microtubules and FtsZ, exhibit this important feature^{2–6}.

From a physics point of view, treadmilling has been often modelled as self-propulsion, where the filament centre of mass moves directionally with a certain velocity to mimic the directional filament growth^{7–9}. While this approach can be appropriate for describing single-filament dynamics, when it comes to the assembly into higher order dynamic structures, self-propelled models might not be suitable. Such models fail to capture the characteristic constant turnover of components in treadmilling systems and by introducing propelling forces may overestimate the forces generated by filament polymerization on obstacles, which have been shown to be small or negligible¹⁰ and instead likely

operate via a ratchet-like interplay between polymerization and thermal fluctuations¹¹. The self-organization mechanisms of treadmilling polymers may hence be different from those of self-propelled filaments and remain unexplored.

Here we develop a computational model for the collective behaviour of treadmilling filaments, accounting for the kinetics of nucleation, growth and shrinkage, to study their collective dynamics. We focus on investigating the self-organization of FtsZ filaments, a highly conserved tubulin homologue¹², widely present in bacteria and one of the best characterized treadmilling systems in the literature^{13–16}. Our model allows us to explore the interplay between polymerization dynamics and collective filament organization at the cellular scale and to directly compare to *in vitro* and *in vivo* experiments. Treadmilling FtsZ filaments self-organize into a dynamic ring¹⁷ in the middle of bacterial cells (the ‘Z-ring’) that orchestrates bacterial cell division^{18–20}. Treadmilling has been shown to be essential for cell division of *Escherichia coli*, *Bacillus subtilis*, *Staphylococcus aureus* and *Streptococcus pneumoniae*^{15,16,21,22}, and in *B. subtilis*, it has been shown to be required for the formation of a coherent Z-ring²³. However, how treadmilling

¹Institute of Science and Technology Austria, Klosterneuburg, Austria. ²Department of Physics and Astronomy, Institute for the Physics of Living Systems, University College London, London, UK. ³Centre for Bacterial Cell Biology, Biosciences Institute, Newcastle University, Newcastle upon Tyne, UK. ⁴Archaea Biology and Ecogenomics Unit, Department of Functional and Evolutionary Ecology, University of Vienna, Vienna, Austria. ⁵School of Life Sciences, The University of Warwick, Coventry, UK. ✉e-mail: andela.saric@ist.ac.at

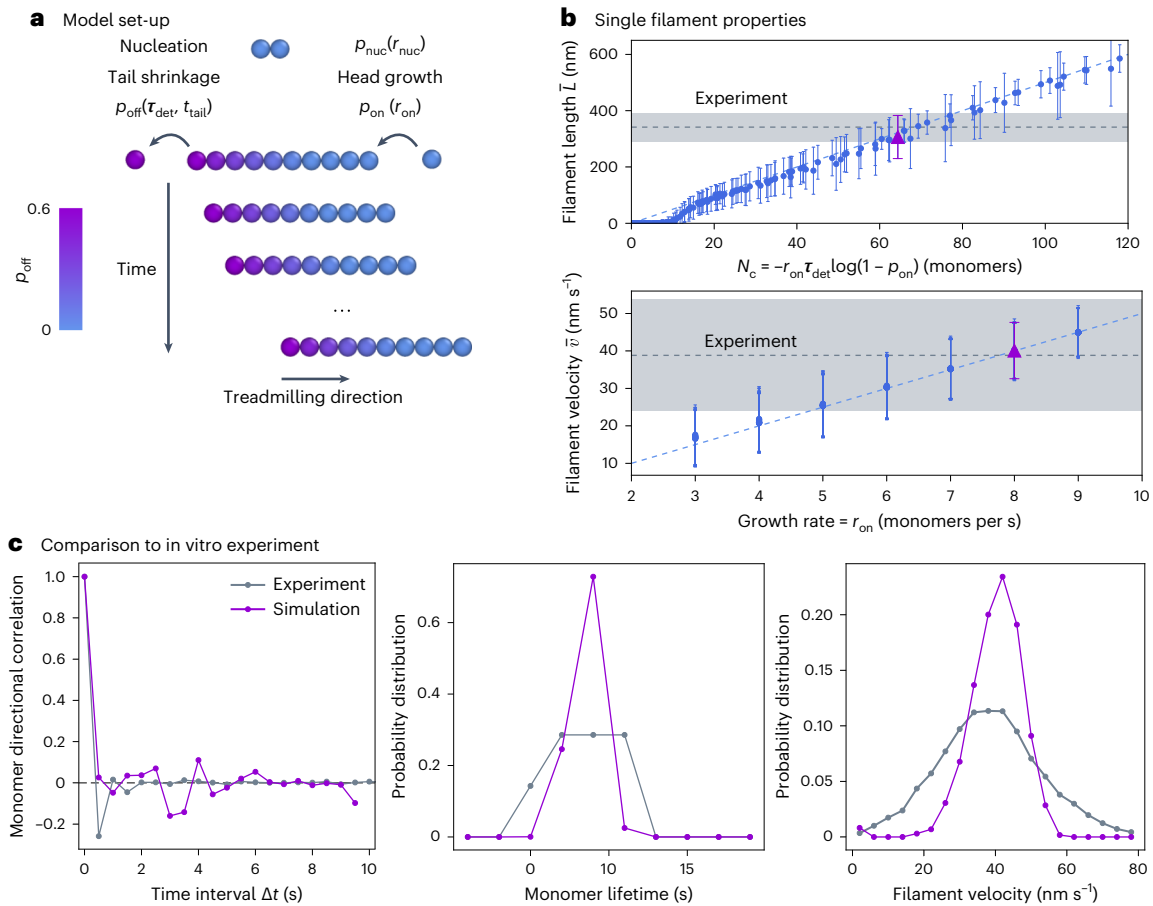


Fig. 1 | Coarse-grained model for treadmilling filaments. **a**, New filaments nucleate at a constant rate r_{nuc} , grow with probability $p_{\text{on}} = r_{\text{on}}dt$ and shrink with probability p_{off} , determined by the monomer detachment time τ_{det} and the time the monomer has been in the system. This growth and shrinkage dynamics results in the apparent directional motion of the filaments over time. **b**, Upper, single filament length against the corresponding intrinsic size N_c . The blue dashed line is the theoretical $\bar{L} = N_c(\sigma = 5 \text{ nm})$. Lower, average treadmilling velocity \bar{v} of a filament against the corresponding growth rate r_{on} . The blue dashed line is the theoretical $\bar{v} = r_{\text{on}}\sigma$. In both graphs, each point is the steady-state average over 20 replicas of single-filament simulations with error

bars for the standard error of the average. The grey dashed lines correspond to the fluorescence microscopy experiments of in vitro reconstituted *E. coli* FtsZ treadmilling filaments on SLBs at 1.25 μM (shaded areas for error). Purple triangles correspond to $r_{\text{on}} = 8$ monomers per second and $\tau_{\text{det}} = 5$ s, which fit experimental measurements best and are used for the simulation data in **c**. **c**, Single-filament dynamics in simulations (in purple) quantitatively matches in vitro FtsZ dynamics (in grey). Left, directional autocorrelation of FtsZ monomers at increasing time intervals Δt decays quickly, showing the static nature of individual monomers. Middle, monomer lifetime distribution. Right, treadmilling filament velocity distribution.

contributes to the self-organization of individual filaments into a large-scale cytoskeletal structure remains unclear.

We first show that our model correctly reproduces single-filament treadmilling dynamics collected in vitro¹³ and proposed in previous theoretical kinetic studies²⁴. We then demonstrate that treadmilling polymers collectively align due to shrinkage and ‘death’ of misaligned filaments, yielding quantitative matching with high-speed atomic force microscopy (HS-AFM) imaging of reconstituted FtsZ filaments. Finally, we find that such a system forms tight ordered dynamic rings when under external biases present in bacterial division. The model quantitatively explains the time-dependent in vivo dynamics of Z-ring condensation and maturation^{23,25} in *B. subtilis*. These results identify a mechanism for ordering of cytoskeletal filaments through dynamic growing and shrinking, which is responsible for the formation of the bacterial division ring and potentially present in a plethora of other cytoskeletal processes across the tree of life.

Model description

We model treadmilling filaments as coarse-grained polymers made of spherical beads with diameter σ (the simulation unit of length) on a two-dimensional plane with periodic boundary conditions²⁶. Individual

beads correspond to distinct monomers, with $\sigma = 5 \text{ nm}$ as known for FtsZ^{19,27,28}. Filaments are formed by connecting monomers via harmonic springs and angle potentials to capture filament stiffness (see Supplementary Information for more details). We time-evolve our system in molecular dynamics simulations and impose filament nucleation, growth and shrinkage kinetics by dynamically creating and deleting monomers in the system (Fig. 1a and Supplementary Video 1; see Supplementary Information for more details).

Treadmilling filaments are active, dissipating energy via nucleotide hydrolysis at the monomer–monomer interface. This results in a change in the interface domains of the monomers, which then tend to dissociate when they reach the tail of the filament^{24,29–31}. To capture these properties, we consider reactions at time intervals $dt_{\text{react}} = 0.1 \text{ s}$ during which individual filaments grow and shrink with probabilities p_{on} and p_{off} respectively, and new filaments are nucleated with probability p_{nuc} . Treadmilling depends only on two parameters: the head polymerization rate, r_{on} , and the typical time over which monomers become available for detachment as a result of hydrolysis, τ_{det} . Here r_{on} (in monomers per second) captures both the bulk free monomer concentration, which we assume is constant, and the polymerization rate constant, such that $p_{\text{on}} = r_{\text{on}}dt_{\text{react}}$. Monomers in solution are thus

implicitly considered. Importantly, filament polymerization is allowed only if free space for monomer addition is available around the filament head. Tail depolymerization is modelled through $p_{\text{off}} = 1 - e^{-t_{\text{tail}}/\tau_{\text{det}}}$, where τ_{det} (in seconds) effectively accounts for both the slow nucleotide hydrolysis at the monomer–monomer interface in the filament and the fast monomer dissociation at the filament tail, while t_{tail} is the time for which the tail monomer has been in the system (see Supplementary Fig. 3 for a detailed exploration of the hydrolysis and dissociation reactions). Given that monomers detach into solution upon depolymerization, p_{off} is not dependent on the environment of the filament on the surface³². To reach steady state, $p_{\text{on}} = p_{\text{off}}$ must be satisfied, which defines an intrinsic size $N_c = -r_{\text{on}}\tau_{\text{det}} \log(1 - p_{\text{on}})$ around which filaments fluctuate while treadmilling at constant velocity $v_c = r_{\text{on}}\sigma$. This also defines a typical monomer lifetime $\tau_c = -\tau_{\text{det}} \log(1 - p_{\text{on}})$. Finally, insertion of new filament nuclei into the system (modelled as dimers) is controlled by the imposed nucleation rate r_{nuc} (in nuclei per second), such that $p_{\text{nuc}} = r_{\text{nuc}}dt_{\text{react}}$. Like the growth rate, r_{nuc} captures both the nucleation rate constant and the free monomer concentration.

Single-filament dynamics

We first perform simulations of individual filaments for a range of filament growth and detachment time parameter sets $\{r_{\text{on}}, \tau_{\text{det}}\}$. We initialize the system with a single filament nucleus and let it evolve in time (Supplementary Video 1). As expected, filaments reach a steady state where they fluctuate around a constant length and treadmilling velocity (Fig. 1b), while the individual monomers display finite lifetimes (Supplementary Figs. 4 and 5). Experimentally, FtsZ protofilaments have been measured (in vivo and in vitro) to be between 100 and 500 nm long and to treadmill at speeds between 15 and 50 nm s⁻¹, while individual monomers turnover at lifetimes around 8 s, depending on the bacterial strain and conditions^{25,28,33–35}, all of which are well within the range we observe in simulations (Fig. 1b).

We now turn to a direct comparison of our model with experiments. For this purpose, we reconstituted *E. coli* FtsZ filaments (FtsA and fluorescently labelled FtsZ) on supported lipid bilayers (SLBs) with excess adenosine triphosphate and guanosine triphosphate and used total internal reflection fluorescence microscopy to image treadmilling dynamics and filament organization (see Supplementary Information for further details). Using previously developed image analysis software^{36,37} we measure filament lengths and velocities (grey dashed lines and shaded regions in Fig. 1b, also reported in ref. 36) as well as individual monomer lifetimes (Supplementary Figs. 4 and 5). When choosing $\{r_{\text{on}}, \tau_{\text{det}}\}$ model parameters that match this specific experimental system (the purple triangles in Fig. 1b), the velocity and lifetime distributions also display a good agreement with the experimental data (Fig. 1c, middle and right).

Importantly, the directional autocorrelation function of individual monomers for different time intervals Δt , measured both in simulations and in in vitro experiments, presents a sharp decay to zero (Fig. 1c, left), indicating that individual monomers remain static even though the filament as a whole appears to be moving. The same is also clearly visible from the individual molecule track analysis in vitro (Supplementary Fig. 7). This lack of motility is an important feature of treadmilling filaments, which also suggests that modelling treadmilling as self-propulsion is likely unsuitable, as individual monomers do not display any directional motion. Consequently, pushing forces exerted by treadmilling filaments might be small, as previously discussed for actin bundles¹⁰. Together, these results demonstrate that our model correctly captures the main aspects of treadmilling dynamics on biologically relevant time and length scales and that it can be benchmarked for a specific protein under particular conditions and used for quantitative comparison with experiments.

Collective filament dynamics

We are now in a position to explore the collective dynamics of many treadmilling filaments and how their mortality affects the formation of higher order structures. We nucleate filaments in the system, characterized by parameters $\{r_{\text{on}}, \tau_{\text{det}}\}$, at a constant nucleation rate r_{nuc} . The system generally reaches steady-state surface density ρ and average filament size \bar{N} while the filament population undergoes continuous turnover (Supplementary Fig. 8). We observe three different collective regimes (Fig. 2a), which depend exclusively on the treadmilling kinetics or the resulting intrinsic filament size N_c (Supplementary Figs. 8–10).

The first regime occurs for very low values of the intrinsic filament size N_c (grey area in Fig. 2a), where individual filaments die out rapidly (Supplementary Fig. 6), resulting in a quasi-zero surface density (Supplementary Figs. 8–10). As the intrinsic filament size increases ($N_c \approx 10$) the system transitions into an unstable treadmilling regime, where filament size fluctuations are comparable to their size (Supplementary Fig. 6). The system is then populated by treadmilling filaments that stochastically emerge and disappear, never reaching high surface densities (pink region in Fig. 2a and Supplementary Video 2). Finally, for higher values of N_c ($N_c \gg 10$), the intrinsic size fluctuations become negligible compared to the filament size (Supplementary Fig. 6), and filaments enter a highly stable and persistent treadmilling regime in which they can achieve long lifetimes. This allows the system to build up its filament population and reach higher surface densities (Supplementary Figs. 8–10).

We find that the majority of this parameter space is characterized by the emergence of a large-scale nematic order (Fig. 2a,b) and the formation of polar bands (snapshots in Fig. 2b and Supplementary Video 3). This behaviour is highly reminiscent of the nematic laning phase previously observed in self-propelled rods^{38,39} and is similarly characterized by high values of local and global nematic order parameter S and high local but low global values of the polar order parameter due to lanes formation (Supplementary Fig. 13). Unlike in self-propelled^{8,38,39} or passive^{40,41} nematic systems, where the system density determines the ordering, in a treadmilling system the turnover kinetics (characterized by N_c) dictates the emergent steady-state ordering and density (Fig. 2b and Supplementary Fig. 10). We find that if monomer hydrolysis and hence treadmilling are arrested and the filaments grow long, the system will evolve towards a highly populated but disordered configuration (Fig. 2d, Supplementary Fig. 15 and Supplementary Video 4). This occurs because, while thermal fluctuations and collisions can foster local alignment and bundling, the system cannot resolve the nematic defects that stochastically arise as filaments nucleate. Hence, treadmilling serves as an effective mechanism for defect healing.

We now turn to a comparison of collective ordering with experiment. As shown in Fig. 2b, HS-AFM images of *E. coli* FtsZ filaments on a SLB bear a striking resemblance to simulation snapshots, with an evident transition to a high nematic order as the system becomes more populated (Supplementary Video 5). These high-resolution images allow us to quantify both the orientational order and the surface density of the system at any time from vector field analysis (Supplementary Fig. 16), enabling a quantitative comparison with the simulations. Figure 2b demonstrates that both HS-AFM and simulation trajectories display the same coupling between orientational order and density, independent of the specific kinetic parameters used. Furthermore, when we perform HS-AFM with a FtsZ mutant with reduced GTPase activity and greatly inhibited depolymerization (FtsZ L169R)⁹, we observe that, just like in simulations, nematic defects are not resolved over time and the system remains at lower nematic order than wild type (Fig. 2d and Supplementary Video 6). These results indicate that our model correctly describes FtsZ treadmilling behaviour as observed experimentally and should therefore provide insight into the mechanisms underlying filament ordering.

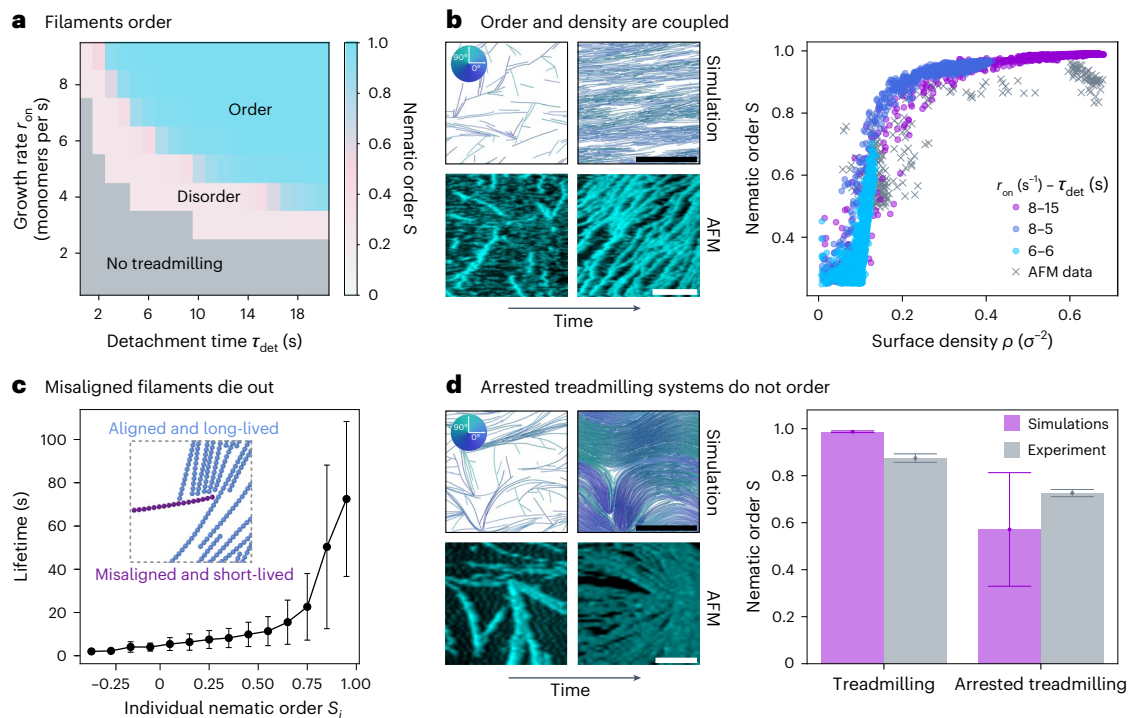


Fig. 2 | Collective behaviour of treadmilling filaments. **a**, Steady-state nematic order parameter S measured in simulations (average over $N = 10$ replicas, $t > 10$ min). Grey indicates the quasi-empty systems of non-treadmilling filaments, blue the nematic order system with polar bands and pink the disordered transitional region. **b**, Left, snapshots of treadmilling systems at early (leftmost column) and late (rightmost column) times in simulations and in HS-AFM experiments (filaments are coloured according to their orientation—see the colour wheel in the inset). Right, nematic order S plotted against surface density ρ at different points in time for reconstituted FtsZ on SLBs (AFM data is shown as crosses) and simulations (coloured according to kinetics and shown as circles). For experiments, data from $N = 3$ different videos is shown. For simulations, $N = 10$ different trajectories are shown for each parameter set. **c**, Filament lifetime for different levels of alignment (characterized by the individual nematic order S_i). We consider only simulations for $N_c \geq 100$ ($N = 10$

replicas per parameter set), which results in 226,077 data points (filaments) in total, binned in S_i with width 0.1. Points correspond to the mean of the bin and the error bar to the standard deviation. Inset, snapshot of a trapped misaligned filament (purple) that dissolves over time (Supplementary Video 7). **d**, Left, snapshots of systems with arrested treadmilling at early (leftmost column) and late (rightmost column) times in simulations (same kinetic parameters as in **b** and in HS-AFM experiments). Right, steady-state nematic order S for treadmilling and non-treadmilling systems. Bars and dots indicate the average for $t > 600$ s ($N = 10$ replicas in simulations: $n = 600$ data points in simulations, $n = 28$ data points for treadmilling experiments and $n = 48$ for arrested treadmilling experiments), and error bars indicate the standard deviation. In experiments, ‘treadmilling’ corresponds to wild-type data and ‘arrested treadmilling’ to the L169R mutant. Unless stated otherwise, simulation data corresponds to $r_{on} = 8 \text{ s}^{-1}$, $\tau_{det} = 15 \text{ s}$ and $r_{nuc} = 1 \text{ s}^{-1}$ for $l_p = 10 \text{ }\mu\text{m}$ and $D = 100 \text{ nm}^2 \text{ s}^{-1}$. Scale bars, 500 nm.

In simulations, we find that the ordering transition is driven by filaments growing against each other, which eventually selects for a common alignment direction, like in systems of self-propelled rods^{38,39,42}. However, the underlying mechanism is completely different: unlike self-propelled rods that exert force when collided with another filament^{43–46}, treadmilling filaments stop growing when they reach another object, but still continue to depolymerize, which results in shrinkage, reorientation or even dissolution of the filaments. Ultimately, the fact that shrinkage is independent of growth causes misaligned filaments to die out, because they are more likely to grow against the neighbours than their aligned counterparts. Supplementary Video 7 exemplifies a striking example of such a filament which, by being misaligned with its surroundings, stops growing and eventually dies.

Figure 2c measures the lifetime of each filament against its average alignment, characterized by the individual nematic order S_i . These two variables are indeed highly correlated: only very aligned filaments ($S_i \approx 1$) reach long lifetimes, up to several minutes, while strongly misaligned polymers die out after a few seconds on average and are gradually replaced with aligned ones. The aligned filaments also treadmill with a velocity that approaches their single-filament value $v_c = r_{on}\sigma$, while the misaligned filaments typically have vanishing velocities (Supplementary Fig. 11). Globally, this behaviour results in the progressive selection of the more stable filaments that align with the rest of the system, reminiscent of what was previously proposed for plant

microtubules^{47,48}. The filament death and birth mechanism and the establishment of order are not rapid but require turnover of a large number of filaments and typically take minutes (Supplementary Fig. 12).

Treadmilling drives bacterial division ring condensation

To showcase the importance of the identified self-organization mechanism in living cells, we investigate the role of treadmilling for bacterial division ring formation. Our *in vivo* experiments recently showed that treadmilling dynamics of FtsZ is essential for Z-ring formation in division of *B. subtilis*²³, but the details linking the two remain elusive. We now use our coarse-grained molecular model for treadmilling filaments to explore the underlying mechanism. Bacterial FtsZ has been observed to display mild natural curvature in live cells and *in vitro*, with diameters similar to or smaller than typical cell diameters^{13,32,49,50}. In addition, its membrane anchor FtsA—which makes composite polymers with FtsZ—forms intrinsically curved filaments that therefore display a preference for curved surfaces⁵¹. This suggests that the interplay between cell geometry and curvature of the (composite) filament should favour filament alignment along the circumference of the cell, similar to what has been previously shown for MreB filaments^{52–54}. We incorporate this curvature-sensing mechanism in the model, as shown in Fig. 3a, by adding a circumference aligning force f_{curv} to the head and tail monomers of each filament (Supplementary Information). We find that a small force of this kind ($f_{curv} = 5k_B T/\sigma$, where k_B is the Boltzmann constant and T is

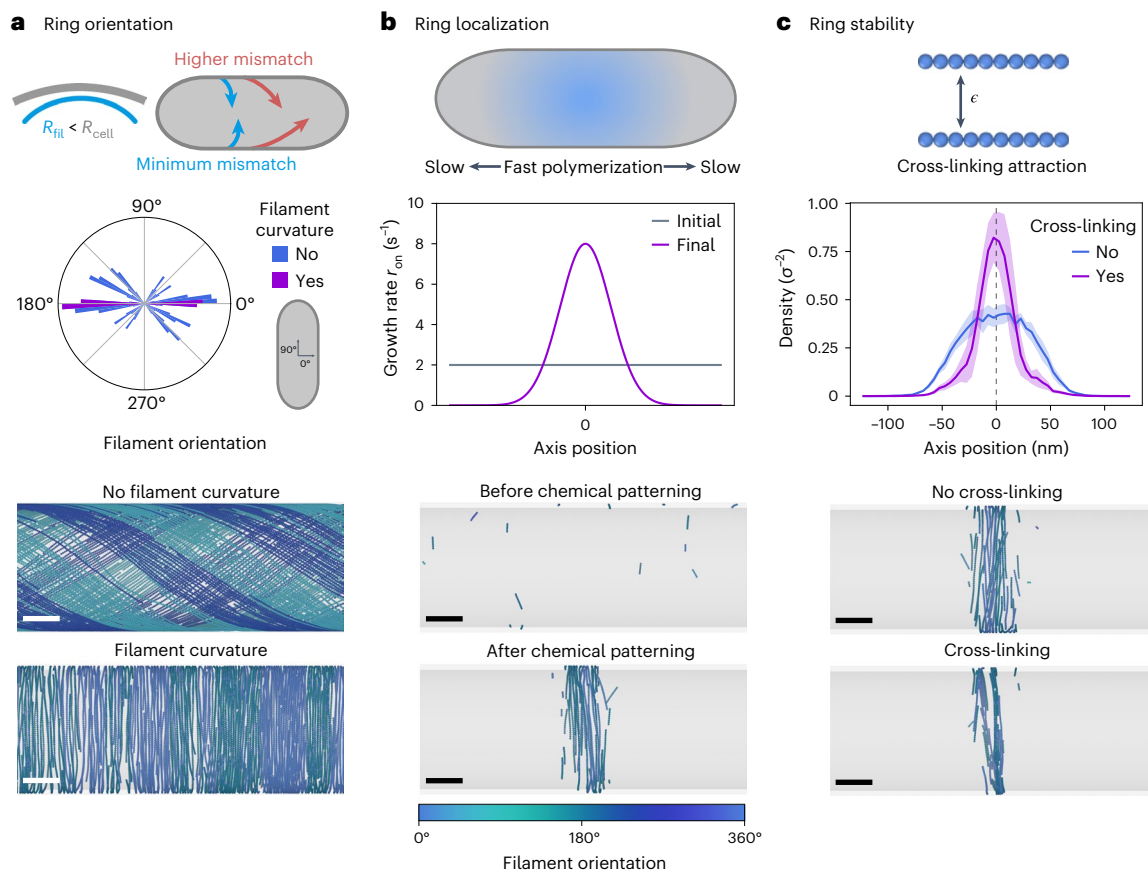


Fig. 3 | Formation of the bacterial division ring. a, Filament curvature and cell geometry drive the collective filament orientation along the cell circumference. Top, illustration of the curvature-sensing mechanism of FtsZ and FtsA filaments. Middle, measured distribution of filament orientations with and without filament curvature. Each bar plot corresponds to the average over $N = 10$ replicas in the nematic order region of the parameter space ($r_{on} = 8 \text{ s}^{-1}$, $\tau_{det} = 15 \text{ s}$). Bottom, two representative snapshots of steady-state configurations of treadmilling filaments with and without filament curvature. **b**, Spatial modulation of FtsZ's growth and nucleation kinetics mediates its midcell localization. Top, illustration of the typical FtsZ kinetics modulation observed in vivo. Middle, example of a kinetics modulation combining an increase in the growth and nucleation rates around the midcell with a decrease at the poles. Bottom, two representative snapshots of system configurations before and after

the modulation of the kinetics is switched on. **c**, Attractive interactions stabilize the ring and mediate tight packing. Top, illustration of the cross-linking implementation. Middle, late time ($t > 8$ minutes after the switch) density profiles along the cell axis with and without cross-linking interactions. The solid lines represent the mean over $N = 10$ replicas and the shaded region, the standard deviation. Bottom, two representative snapshots of steady-state rings with and without cross-linking interactions. In **b** and **c** we use switch parameters $r_{on}^0 = 2 \text{ s}^{-1}$, $r_{on}^1 = 8 \text{ s}^{-1}$ and $w_{prof} = 100 \text{ nm}$ for $\tau_{det} = 15 \text{ s}$, where w_{prof} defines the profile width (see Supplementary Information). In all snapshots, the filaments are coloured according to their orientation with respect to the cell circumference (see colour bar at the bottom). For all simulations, we set $f_{curv} = 5k_B T/\sigma$, $l_p = 10 \mu\text{m}$ and $D = 100 \text{ nm}^2 \text{ s}^{-1}$ in a box of size $L = 200 \sigma = 1 \mu\text{m}$. Scale bars, 50 nm.

the temperature) is sufficient to determine the global orientation of the filaments along the cell circumference (Fig. 3a), highlighting the importance of the interplay between filament and cellular geometry in supramolecular organization.

Bacteria have evolved a number of different molecular tools that act in complementary ways to position FtsZ filaments to the right division site—the midcell—at the right time. Such systems include dynamic chemical patterning^{55–60} and condensate formation⁶¹ or nucleoid occlusion^{62–65} and generally have the effect of spatially modulating FtsZ polymerization, resulting in higher density of filaments at the midcell and lower density around the poles (schematic in Fig. 3b). This effect can be captured by incorporating higher polymerization rates at the midcell and lower rates around the poles. Our model can incorporate this FtsZ growth modulation as an instantaneous change from a uniform distribution along the cell body to a Gaussian profile centred at the midcell for growth and nucleation rates, with a constant detachment time (Fig. 3b and Supplementary Information). We find that the resulting combination of midcell enrichment and cell pole depletion of FtsZ proteins reliably localizes the filaments to the midcell region (Fig. 3b).

Finally, we consider one more model ingredient. It has been shown that FtsZ self-interaction, as well as cross-linking by FtsZ-binding proteins such as ZapA, can promote Z-ring condensation and that cross-linker deletion can lead to axial spreading of the rings^{25,36,66,67}. In line with this, we find that including explicit attractive interactions between filaments has an important stabilizing effect on the ring structure, further promoting filament alignment and tight packing and allowing for a sustained monomer accumulation in the ring over time (Fig. 3c and Supplementary Fig. 18). Taken together, these results show that treadmilling filaments in our model can spontaneously form stable ring-like structures when a combination of filament curvature, attractive interfilament interactions and spatio-temporal modulation of the filament kinetics are considered.

Comparison with in vivo data

We are now in a good position to compare our model for Z-ring formation with live-cell data. Our experiments have previously directly identified a very particular dynamics of Z-ring formation in living *B. subtilis*

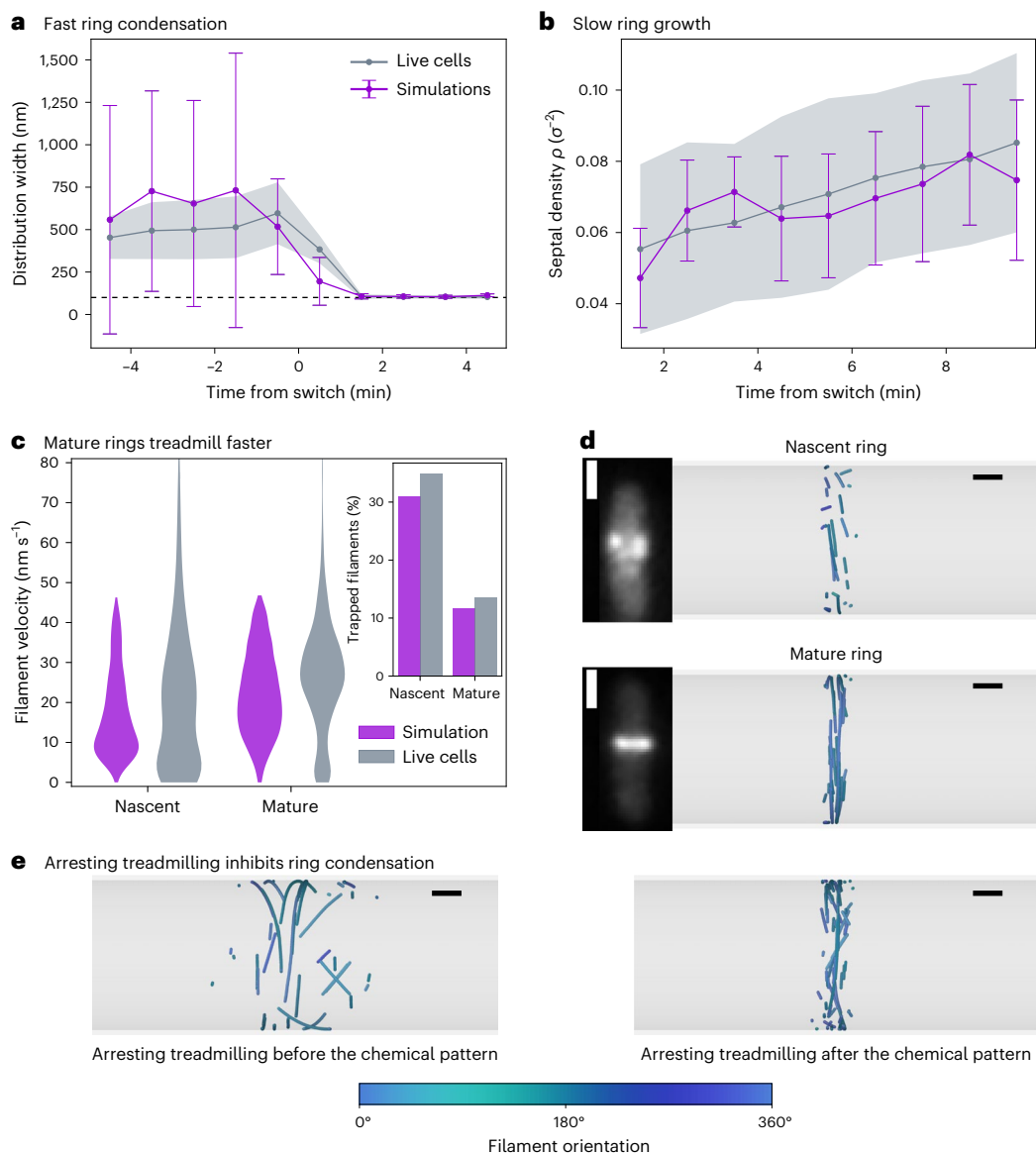


Fig. 4 | Z-ring formation in vivo. **a**, Z-ring condensation dynamics for live cells (grey) and simulations (purple). A rapid ring collapse around $t = 0$ minutes is observed. **b**, Ring density in time for live cells (grey) and simulations (purple). A positive average slope is observed, indicating the slow accumulation of proteins to the division site. In **a** and **b**, solid lines correspond to the average over samples ($N = 10$ replicas for simulations, $N = 67$ cells analysed from three independently prepared bacterial samples) and the shaded region or error bars to the standard deviation. Time $t = 0$ corresponds to the onset of the chemical pattern. **c**, Filament velocity distributions in nascent and mature rings for live cells (grey) and simulations (purple). Inset, fraction of trapped filaments ($v < 10 \text{ nm s}^{-1}$) for each distribution. In simulations we define $t < 2 \text{ min}$ for nascent and $t > 8 \text{ min}$ for mature rings. Statistics are done over $n = 1,834$ data points (filaments) for simulated nascent rings, $n = 2,347$ data points (filaments) for simulated mature rings, $n = 1,066$ data points for nascent in vivo rings and $n = 3,126$ data points for

mature in vivo rings (note that this is the number of filaments imaged but the number of cells is $N = 67$ biological replicates). **d**, Representative snapshots of two successive ring configurations observed in vivo and in simulations. Microscopy images show fluorescently tagged FtsZ in live *B. subtilis* cells. These experiments were repeated independently with similar results. Simulations were repeated for $N = 10$ replicas with similar results. **e**, Representative snapshots of systems at $t = 10 \text{ min}$ after arresting treadmilling. Treadmilling is arrested 5 min before (left) and 1 min after (right) the onset of the chemical pattern that modulates the growth kinetics. The simulation data in **a**, **b** and **c** correspond to a switch with parameters $r_{\text{on}}^0 = 2 \text{ s}^{-1}$, $r_{\text{on}}^1 = 9 \text{ s}^{-1}$ and $r_{\text{nuc}}^1 = 2 \text{ s}^{-1}$ for $\tau_{\text{det}} = 15 \text{ s}$ and $w_{\text{prof}} = 100 \text{ nm}$. Note that monomers in simulations are rendered with size 20 nm instead of the actual 5 nm for visualization purposes and are coloured according to their orientation with respect to the cell circumference (see the colour bar at the bottom). Scale bars, $1 \mu\text{m}$ (**d**, insets), 200 nm (**d**, **e**).

cells: localization of the ring to the midcell, often referred to as ring condensation, occurs very rapidly, within one minute (Fig. 4a), while ring maturation (growth and thickening) occurs over several minutes (Fig. 4b). If treadmilling is impaired early on, the Z-ring cannot form and remains diffuse, while impairing treadmilling during maturation disrupts proper division²³. Our experiments also found that the average treadmilling velocity of filaments in mature Z-rings is substantially faster than in nascent ones (Fig. 3c).

To explore whether our model can capture the dynamics of Z-ring formation in vivo and explain the mechanism behind it, we simulate systems on the cell scale ($L = 3 \mu\text{m}$ giving $R \approx 1 \mu\text{m}$). We limit the total amount of monomers to the estimated amount of FtsZ in *B. subtilis* Z-rings $N_{\text{max}} = 2,000$ (Supplementary Information), resulting in a relatively low monomer surface density. Strikingly, as shown in Fig. 4a and Supplementary Video 8, our model also displays rapid ring condensation, which occurs only a few seconds after the switch of the

modulation profile. This behaviour is caused by the rapid dying out of the filaments in the growth-inhibited areas of the cell, as their depolymerization rate is faster than the polymerization rate. The whole process occurs on the scale of the single monomer's lifetime, as controlled by τ_{det} . Hence, treadmilling allows the system to rapidly respond to external chemical cues.

We further find, in agreement with live-cell experiments, that after rapid ring condensation at the site of division, treadmilling filaments in the model accumulate rather slowly, over a time-span of several minutes. The simulations reveal a steadily increasing surface density of monomers in the midcell region that matches well the experimental measurements (Fig. 4b). This feature is the inherent result of treadmilling-driven alignment: the ring structure transitions from an initially disordered state to an ordered state populated by several bundles of filaments tightly bound together (Fig. 4d and Supplementary Video 8) through the dissolution and replacement of misaligned filaments in a process that is analogous to what we observed in vitro for *E. coli* FtsZ. Mature rings are thus composed of small patches of FtsZ organized in bands that are a few filaments wide and travel together, as previously observed in live-cell imaging^{19,68,69} (Fig. 4d and Supplementary Video 8). These bands are tightly bound, displaying high local density of monomers, consistent with cryotomography experiments estimating an interfilament distance of approximately 6 nm in FtsZ rings⁷⁰.

Ring maturation is driven by the replacement of misaligned filaments, which is at heart a trial-and-error process, rendering this process slow. The decrease in the fraction of low-velocity misaligned filaments in the mature ring also naturally leads to faster treadmilling velocities without individual filaments speeding up, which matches live-cell measurements (Fig. 4c). In other words, the surviving filaments all run parallel to each other with velocities close to maximal values. Finally, we found that arresting treadmilling in our model has similar effects to those observed in vivo. If treadmilling is arrested early on, before the onset of the chemical patterning, the filament population remains diffuse and never condenses to the midcell (Fig. 4e and Supplementary Video 9). If treadmilling is arrested after the switch of the chemical patterning, the ring forms at the midcell, but displays aberrant, 'frozen' configurations (Fig. 4e, Supplementary Fig. 21 and Supplementary Video 10). The crucial role of treadmilling in the positioning of the FtsZ ring that our model reveals has also been previously discussed in the context of *E. coli*: it has been reported that mutants that are insensitive to classical positioning systems like Min (FtsZ2, FtsZ9 and FtsZ100) all have very low or undetectable GTPase activity. This implies that the lack of treadmilling underlies their inability to correctly position the ring²⁸.

Altogether, our treadmilling model naturally reproduces the key dynamical aspects of Z-ring formation observed in live cells. FtsZ filaments are able to localize to the midcell on timescales similar to the monomer lifetimes, driven by the underlying spatial modulation of the polymerization rates, while the tightly packed division rings grow on substantially longer timescales by virtue of misaligned filaments dying and growing again until only the aligned ones remain. This mechanism is at play irrespective of the filament density: simulations of treadmilling filaments on a surface constrained to in-vivo-like low protein concentrations show that ordering still occurs and is driven by the same mechanism of death by misalignment (Supplementary Fig. 14). More generally, our model explains the importance of treadmilling—dynamic growth and shrinkage of filaments—in localizing and timing bacterial division.

Discussion

Our treadmilling model reveals a surprisingly rich collective behaviour arising from the dissolution and replacement of misaligned filaments, characteristic of mortal polymers. These findings put forward treadmilling filaments as a paradigm for a dynamic self-ordering system that

is able to quickly remodel itself in response to external cues. This suggests that both naturally occurring and artificial treadmilling polymers could be a useful tool in areas such as synthetic cell development or programmable active matter, capable of healing via local filament dissolution. For example, microfluidic devices and chemical or photo patterning could be used experimentally to generate and control dynamic treadmilling filament systems.

From a biological perspective, our model provides structural and dynamic insights into functional FtsZ assemblies. The model can further be used to investigate how the dynamics of the Z-ring affects recruitment and activation of bacterial wall synthesis machinery, resulting in the growth of the cell wall at midcell, which ultimately divides the cell into two^{15,16,71–73}.

From a physics point of view, we find that treadmilling filaments belong to a distinct class of active matter, which consumes energy not for motility but for turnover and thus order via death of locally misaligned filaments. This mechanism is expected to have further implications for filament collective behaviour, such as the response to obstacles, perturbations and propagation of information. For instance, treadmilling filaments can be expected to evacuate the region around obstacles due to their mortality, instead of being trapped. Due to filament dissolution, such systems are also expected to locally heal upon defect introduction or external perturbation and are not expected to transduce the perturbation deep into the assembly. Overall, by revealing a distinct ordering mechanism in chemically active matter, our work highlights the importance of exploring the collective and material properties of explicitly mortal filaments.

Online content

Any methods, additional references, Nature Portfolio reporting summaries, source data, extended data, supplementary information, acknowledgements, peer review information; details of author contributions and competing interests; and statements of data and code availability are available at <https://doi.org/10.1038/s41567-024-02597-8>.

References

- Andreu, J. M. How protein filaments treadmill. *Biophys. J.* **119**, 717–720 (2020).
- Wegner, A. Head to tail polymerization of actin. *J. Mol. Biol.* **108**, 139–150 (1976).
- Erlenkämper, C. & Kruse, K. Treadmilling and length distributions of active polar filaments. *J. Chem. Phys.* **139**, 164907 (2013).
- Waterman-Storer, C. M. & Salmon, E. D. Microtubule dynamics: treadmilling comes around again. *Curr. Biol.* **7**, R369–R372 (1997).
- Panda, D., Miller, H. P. & Wilson, L. Rapid treadmilling of brain microtubules free of microtubule-associated proteins in vitro and its suppression by tau. *Proc. Natl Acad. Sci. USA* **96**, 12459–12464 (1999).
- Rzadzinska, A. K., Schneider, M. E., Davies, C., Riordan, G. P. & Kachar, B. An actin molecular treadmill and myosins maintain stereocilia functional architecture and self-renewal. *J. Cell Biol.* **164**, 887–897 (2004).
- Denk, J., Huber, L., Reithmann, E. & Frey, E. Active curved polymers form vortex patterns on membranes. *Phys. Rev. Lett.* **116**, 178301 (2016).
- Shaebani, M. R., Wsocki, A., Winkler, R. G., Gompper, G. & Rieger, H. Computational models for active matter. *Nat. Rev. Phys.* **2**, 181–199 (2020).
- Dunajova, Z. et al. Chiral and nematic phases of flexible active filaments. *Nat. Phys.* **19**, 1916–1926 (2023).
- Footer, M. J., Kerssemakers, J. W. J., Theriot, J. A. & Dogterom, M. Direct measurement of force generation by actin filament polymerization using an optical trap. *Proc. Natl Acad. Sci. USA* **104**, 2181–2186 (2007).
- Theriot, J. A. The polymerization motor. *Traffic* **1**, 19–28 (2000).

12. Nogales, E., Downing, K. H., Amos, L. A. & Löwe, J. Tubulin and FtsZ form a distinct family of GTPases. *Nat. Struct. Biol.* **5**, 451–458 (1998).
13. Loose, M. & Mitchison, T. J. The bacterial cell division proteins FtsA and FtsZ self-organize into dynamic cytoskeletal patterns. *Nat. Cell Biol.* **16**, 38–46 (2014).
14. Ramirez-Diaz, D. A. et al. Treadmilling analysis reveals new insights into dynamic FtsZ ring architecture. *PLoS Biol.* **16**, e2004845 (2018).
15. Bisson-Filho, A. W. et al. Treadmilling by FtsZ filaments drives peptidoglycan synthesis and bacterial cell division. *Science* **355**, 739–743 (2017).
16. Yang, X. et al. GTPase activity-coupled treadmilling of the bacterial tubulin FtsZ organizes septal cell wall synthesis. *Science* **355**, 744–747 (2017).
17. Anderson, D. E., Gueiros-Filho, F. J. & Erickson, H. P. Assembly dynamics of FtsZ rings in *Bacillus subtilis* and *Escherichia coli* and effects of FtsZ-regulating proteins. *J. Bacteriol.* **186**, 5775–5781 (2004).
18. Barrows, J. M. & Goley, E. D. FtsZ dynamics in bacterial division: what, how, and why? *Curr. Opin. Cell Biol.* **68**, 163–172 (2021).
19. McQuillen, R. & Xiao, J. Insights into the structure, function, and dynamics of the bacterial cytokinetic FtsZ-ring. *Annu. Rev. Biophys.* **49**, 309–341 (2020).
20. Mahone, C. R. & Goley, E. D. Bacterial cell division at a glance. *J. Cell Sci.* **133**, jcs237057 (2020).
21. Monteiro, J. M. et al. Peptidoglycan synthesis drives an FtsZ-treadmilling-independent step of cytokinesis. *Nature* **554**, 528–532 (2018).
22. Perez, A. J. et al. Movement dynamics of divisome proteins and PBP2x: FtsW in cells of *Streptococcus pneumoniae*. *Proc. Natl Acad. Sci. USA* **116**, 3211–3220 (2019).
23. Whitley, K. D. et al. FtsZ treadmilling is essential for Z-ring condensation and septal constriction initiation in *Bacillus subtilis* cell division. *Nat. Commun.* **12**, 2448 (2021).
24. Corbin, L. C. & Erickson, H. P. A unified model for treadmilling and nucleation of single-stranded FtsZ protofilaments. *Biophys. J.* **119**, 792–805 (2020).
25. Squyres, G. R. et al. Single-molecule imaging reveals that Z-ring condensation is essential for cell division in *Bacillus subtilis*. *Nat. Microbiol.* **6**, 553–562 (2021).
26. Hafner, A. E., Krausser, J. & Šarić, A. Minimal coarse-grained models for molecular self-organisation in biology. *Curr. Opin. Struct. Biol.* **58**, 43–52 (2019).
27. Löwe, J. & Amos, L. A. Crystal structure of the bacterial cell-division protein FtsZ. *Nature* **391**, 203–206 (1998).
28. Erickson, H. P., Anderson, D. E. & Osawa, M. FtsZ in bacterial cytokinesis: cytoskeleton and force generator all in one. *Microbiol Mol. Biol. Rev.* **74**, 504–28 (2010).
29. Wagstaff, J. M. et al. A polymerization-associated structural switch in FtsZ that enables treadmilling of model filaments. *mBio* **8**, e00254-17 (2017).
30. Ruiz, F. M. et al. FtsZ filament structures in different nucleotide states reveal the mechanism of assembly dynamics. *PLoS Biol.* **20**, e3001497 (2022).
31. Du, S., Pichoff, S., Kruse, K. & Lutkenhaus, J. FtsZ filaments have the opposite kinetic polarity of microtubules. *Proc. Natl Acad. Sci. USA* **115**, 10768–10773 (2018).
32. Radler, P. et al. In vitro reconstitution of *Escherichia coli* divisome activation. *Nat. Commun.* **13**, 2635 (2022).
33. Li, Z., Trimble, M. J., Brun, Y. V. & Jensen, G. J. The structure of FtsZ filaments in vivo suggests a force-generating role in cell division. *EMBO J.* **26**, 4694–4708 (2007).
34. Chen, Y. & Erickson, H. P. Rapid in vitro assembly dynamics and subunit turnover of FtsZ demonstrated by fluorescence resonance energy transfer. *J. Biol. Chem.* **280**, 22549–22554 (2005).
35. Huecas, S. et al. Energetics and geometry of FtsZ polymers: Nucleated self-assembly of single protofilaments. *Biophys. J.* **94**, 1796–1806 (2008).
36. Caldas, P. et al. Cooperative ordering of treadmilling filaments in cytoskeletal networks of FtsZ and its crosslinker ZapA. *Nat. Commun.* **10**, 5744 (2019).
37. Caldas, P., Radler, P., Sommer, C. & Loose, M. in *Methods in Cell Biology* Vol. 158 (ed. Tran, P.) 145–161 (Academic, 2020).
38. Shi, X. & Chaté, H. Self-propelled rods: linking alignment-dominated and repulsion-dominated active matter. Preprint at <https://doi.org/10.48550/arXiv.1807.00294> (2018).
39. Großmann, R., Aranson, I. S. & Peruani, F. A particle-field approach bridges phase separation and collective motion in active matter. *Nat. Commun.* **11**, 5365 (2020).
40. Onsager, L. The effects of shape on the interaction of colloidal particles. *Ann. N. Y. Acad. Sci.* **51**, 627–659 (1949).
41. Tjipito-Margo, B. & Evans, G. T. The Onsager theory of the isotropic-nematic liquid crystal transition: incorporation of the higher virial coefficients. *J. Chem. Phys.* **93**, 4254–4265 (1990).
42. Perepelitsa, M., Timofeyev, I., Murphy, P. & Igoshin, O. A. Mean-field model for nematic alignment of self-propelled rods. *Phys. Rev. E* **106**, 34613 (2022).
43. Schaller, V., Weber, C., Semmrich, C., Frey, E. & Bausch, A. R. Polar patterns of driven filaments. *Nature* **467**, 73–77 (2010).
44. Sciortino, A. & Bausch, A. R. Pattern formation and polarity sorting of driven actin filaments on lipid membranes. *Proc. Natl Acad. Sci. USA* **118**, e2017047118 (2021).
45. Henkin, G., DeCamp, S. J., Chen, D. T. N., Sanchez, T. & Dogic, Z. Tunable dynamics of microtubule-based active isotropic gels. *Trans. R. Soc. A* **372**, 20140142 (2014).
46. DeCamp, S. J., Redner, G. S., Baskaran, A., Hagan, M. F. & Dogic, Z. Orientational order of motile defects in active nematics. *Nat. Mater.* **14**, 1110–1115 (2015).
47. Dixit, R. & Cyr, R. Encounters between dynamic cortical microtubules promote ordering of the cortical array through angle-dependent modifications of microtubule behavior. *Plant Cell* **16**, 3274–3284 (2004).
48. Tindemans, S. H., Hawkins, R. J. & Mulder, B. M. Survival of the aligned: ordering of the plant cortical microtubule array. *Phys. Rev. Lett.* **104**, 058103 (2010).
49. Erickson, H. P. Modeling the physics of FtsZ assembly and force generation. *Proc. Natl Acad. Sci. USA* **106**, 9238–9243 (2009).
50. Ghosh, B. & Sain, A. Origin of contractile force during cell division of bacteria. *Phys. Rev. Lett.* **101**, 178101 (2008).
51. Nierhaus, T. et al. Bacterial divisome protein FtsA forms curved antiparallel double filaments when binding to FtsN. *Nat. Microbiol.* **7**, 1686–1701 (2022).
52. Ouzounov, N. et al. MreB orientation correlates with cell diameter in *Escherichia coli*. *Biophys. J.* **111**, 1035–1043 (2016).
53. Hussain, S. et al. MreB filaments align along greatest principal membrane curvature to orient cell wall synthesis. *eLife* **7**, e32471 (2018).
54. Shi, H., Quint, D. A., Grason, G. M., Gopinathan, A. & Huang, K. C. Chiral twisting in a bacterial cytoskeletal polymer affects filament size and orientation. *Nat. Commun.* **11**, 1408 (2020).
55. Loose, M., Fischer-Friedrich, E., Ries, J., Kruse, K. & Schwille, P. Spatial regulators for bacterial cell division self-organize. *Science* **320**, 789–792 (2008).

56. Kiekebusch, D., Michie, K. A., Essen, L. O., Löwe, J. & Thanbichler, M. Localized dimerization and nucleoid binding drive gradient formation by the bacterial cell division inhibitor MipZ. *Mol. Cell* **46**, 245–259 (2012).
57. Arumugam, S., Petrášek, Z. & Schwille, P. MinCDE exploits the dynamic nature of FtsZ filaments for its spatial regulation. *Proc. Natl Acad. Sci. USA* **111**, 1192–1200 (2014).
58. Zieske, K. & Schwille, P. Reconstitution of self-organizing protein gradients as spatial cues in cell-free systems. *eLife* **3**, e03949 (2014).
59. Feddersen, H., Würthner, L., Frey, E. & Bramkamp, M. Dynamics of the *Bacillus subtilis* Min system *mBio* **12**, e00296-21 (2021).
60. Corrales-Guerrero, L. et al. MipZ caps the plus-end of FtsZ polymers to promote their rapid disassembly. *Proc. Natl Acad. Sci. USA* **119**, e2208227119 (2022).
61. Ramm, B. et al. Biomolecular condensate drives polymerization and bundling of the bacterial tubulin FtsZ to regulate cell division. *Nat. Commun.* **14**, 3825 (2023).
62. Wu, L. J. & Errington, J. Coordination of cell division and chromosome segregation by a nucleoid occlusion protein in *Bacillus subtilis*. *Cell* **117**, 915–925 (2004).
63. Lutkenhaus, J. Linking DNA replication to the Z ring. *Nat. Microbiol.* **6**, 1108–1109 (2021).
64. Männik, J. & Bailey, M. W. Spatial coordination between chromosomes and cell division proteins in *Escherichia coli*. *Front. Microbiol.* **6**, 306 (2015).
65. Bernhardt, T. G. & De Boer, P. A. J. SlmA, a nucleoid-associated, FtsZ binding protein required for blocking septal ring assembly over chromosomes in *E. coli*. *Mol. Cell* **18**, 555–564 (2005).
66. Buss, J. et al. In vivo organization of the FtsZ-ring by ZapA and ZapB revealed by quantitative super-resolution microscopy. *Mol. Microbiol.* **89**, 1099–1120 (2013).
67. Guan, F. et al. Lateral interactions between protofilaments of the bacterial tubulin homolog FtsZ are essential for cell division. *eLife* **7**, e35578 (2018).
68. Walker, B. E., Männik, J. & Männik, J. Transient membrane-linked FtsZ assemblies precede Z-ring formation in *Escherichia coli*. *Curr. Biol.* **30**, 499–508 (2020).
69. Lyu, Z., Coltharp, C., Yang, X. & Xiao, J. Influence of FtsZ GTPase activity and concentration on nanoscale Z-ring structure in vivo revealed by three-dimensional superresolution imaging. *Biopolymers* **105**, 725–734 (2016).
70. Szwedziak, P., Wang, Q., Bharat, T. A. M., Tsim, M. & Löwe, J. Architecture of the ring formed by the tubulin homologue FtsZ in bacterial cell division. *eLife* **3**, 04601 (2014).
71. McCausland, J. W. et al. Treadmilling FtsZ polymers drive the directional movement of sPG-synthesis enzymes via a Brownian ratchet mechanism. *Nat. Commun.* **12**, 609 (2023).
72. Navarro, P. P. et al. Cell wall synthesis and remodelling dynamics determine division site architecture and cell shape in *Escherichia coli*. *Nat. Microbiol.* **7**, 1621–1634 (2022).
73. Puls, J. S., Brajtenbach, D., Schneider, T., Kubitscheck, U. & Grein, F. Inhibition of peptidoglycan synthesis is sufficient for total arrest of staphylococcal cell division. *Sci. Adv.* **9**, 9023 (2023).
74. Vanhille-Campos, C. et al. Self-organization of mortal filaments and its role in bacterial division ring formation. *University College London* <https://doi.org/10.5522/04/24754527> (2024).
75. Baranova, N. & Loose, M. in *Cytokinesis, Methods in Cell Biology* Vol. 137 (ed. Echarid. A.) Ch. 21 (Elsevier, 2017); <https://doi.org/10.1016/bs.mcb.2016.03.036>
76. Baranova, N. et al. Diffusion and capture permits dynamic coupling between treadmilling FtsZ filaments and cell division proteins. *Nat. Microbiol.* **5**, 407–417, <https://doi.org/10.1038/s41564-019-0657-5> (2020).
77. Vanhille-Campos, C. et al. Treadmilling filaments. *GitHub* <https://github.com/Saric-Group/treadmilling> (2024).

Publisher's note Springer Nature remains neutral with regard to jurisdictional claims in published maps and institutional affiliations.

Open Access This article is licensed under a Creative Commons Attribution 4.0 International License, which permits use, sharing, adaptation, distribution and reproduction in any medium or format, as long as you give appropriate credit to the original author(s) and the source, provide a link to the Creative Commons licence, and indicate if changes were made. The images or other third party material in this article are included in the article's Creative Commons licence, unless indicated otherwise in a credit line to the material. If material is not included in the article's Creative Commons licence and your intended use is not permitted by statutory regulation or exceeds the permitted use, you will need to obtain permission directly from the copyright holder. To view a copy of this licence, visit <http://creativecommons.org/licenses/by/4.0/>.

© The Author(s) 2024

Reporting summary

Further information on research design is available in the Nature Portfolio Reporting Summary linked to this article.

Data availability

The simulation data presented in this work are available from the University College London public data repository at <https://doi.org/10.5522/04/24754527> (ref. 74). Live-cell imaging of FtsZ rings data presented in this work are from ref. 23. High-speed atomic force microscopy data presented in this work are from ref. 9. Total internal reflection fluorescence microscopy data presented in this work are from refs. 37,75,76.

Code availability

Appropriate documentation and example files to replicate the simulation results presented in this work are available from the University College London public data repository at <https://doi.org/10.5522/04/24754527> (ref. 74). A maintained version of the code is available on GitHub⁷⁷. Simulation data analysis was performed using custom Python code, which makes use of several public libraries such as NumPy, pandas or Ovito, also available at ref. 74. ImageJ (current version v.1.54) and Python (current version Jupyter Notebook v.6.5.4) were used for the in vitro data analysis. Live-cell imaging videos were analysed using Fiji (v.1.53 and v.1.54) with open-source plugins PureDenoise, StackReg, MicrobeJ (v.5.131), ilastik (v.1.3.3post2) and custom code available via GitHub at https://github.com/HoldenLab/Ring_Analysis_IJ. Further in vivo data analysis was done using Matlab with custom code available via GitHub at <https://github.com/HoldenLab/ring-fitting2>; <https://github.com/HoldenLab/violinplusDABEST-Matlab> and <https://github.com/HoldenLab/ring-simulator>.

Acknowledgements

We thank I. Palaia (ISTA) for useful discussions and K. Lim and R. W. Wong (WPI-Nano Life Science Institute, Kanazawa University) for

providing access to HS-AFM. We would like to thank B. Prats Mateu (MSD Austria, Vienna) for providing the HS-AFM data. This work was supported by the Royal Society (grant no. UF160266; C.V.-C. and A.Š.), the European Union's Horizon 2020 Research and Innovation Programme (grant no. 802960; A.Š.), the Austrian Science Fund (FWF) Stand-Alone P34607 (M.L.) and a Wellcome Trust and Royal Society Sir Henry Dale Fellowship (grant no. 206670/Z/17/Z; S.H. and K.D.W.).

Author contributions

C.V.-C. and A.Š. designed the research aims. C.V.-C. designed the model and carried out the simulations and data analysis under supervision of A.Š. P.R. designed and performed the in vitro TIRF microscopy experiments under supervision of M.L. K.D.W. reanalysed the in vivo experimental data under supervision of S.H. A.Š. directed the research. C.V.-C. and A.Š. wrote the manuscript, and all authors commented on it.

Competing interests

The authors declare no competing interests.

Additional information

Supplementary information The online version contains supplementary material available at <https://doi.org/10.1038/s41567-024-02597-8>.

Correspondence and requests for materials should be addressed to Anđela Šarić.

Peer review information *Nature Physics* thanks Harold Erickson and the other, anonymous, reviewer(s) for their contribution to the peer review of this work.

Reprints and permissions information is available at www.nature.com/reprints.

Reporting Summary

Nature Portfolio wishes to improve the reproducibility of the work that we publish. This form provides structure for consistency and transparency in reporting. For further information on Nature Portfolio policies, see our [Editorial Policies](#) and the [Editorial Policy Checklist](#).

Statistics

For all statistical analyses, confirm that the following items are present in the figure legend, table legend, main text, or Methods section.

n/a Confirmed

- The exact sample size (n) for each experimental group/condition, given as a discrete number and unit of measurement
- A statement on whether measurements were taken from distinct samples or whether the same sample was measured repeatedly
- The statistical test(s) used AND whether they are one- or two-sided
Only common tests should be described solely by name; describe more complex techniques in the Methods section.
- A description of all covariates tested
- A description of any assumptions or corrections, such as tests of normality and adjustment for multiple comparisons
- A full description of the statistical parameters including central tendency (e.g. means) or other basic estimates (e.g. regression coefficient) AND variation (e.g. standard deviation) or associated estimates of uncertainty (e.g. confidence intervals)
- For null hypothesis testing, the test statistic (e.g. F , t , r) with confidence intervals, effect sizes, degrees of freedom and P value noted
Give P values as exact values whenever suitable.
- For Bayesian analysis, information on the choice of priors and Markov chain Monte Carlo settings
- For hierarchical and complex designs, identification of the appropriate level for tests and full reporting of outcomes
- Estimates of effect sizes (e.g. Cohen's d , Pearson's r), indicating how they were calculated

Our web collection on [statistics for biologists](#) contains articles on many of the points above.

Software and code

Policy information about [availability of computer code](#)

Data collection All the computational data presented in this work was obtained by running Molecular Dynamics simulations on a custom modified version of the LAMMPS software package (September 2021 release). A maintained version of this custom modifications together with some Python scripts to generate the required input files to run the simulations are available for download at the following GitHub repository: <https://github.com/Saric-Group/treadmilling> -- A copy of the current version of this code is also available at the following UCL public data repository: <https://doi.org/10.5522/04/24754527> -- Note that this repository will only be activated upon publication of the work. Both of these repositories also include all necessary instructions to replicate the data presented in this work

Data analysis Simulation data analysis was performed using custom Python code which makes use of several public libraries such as numpy, pandas or ovito. All necessary code to replicate the analysis performed for this work is available for download at the following UCL public data repository: <https://doi.org/10.5522/04/24754527>

ImageJ (current version 1.54) and Python (current version Jupyter Notebook 6.5.4) was used for the in vitro data analysis.

Live cell imaging videos were analysed using Fiji (v1.53 and v1.54) with open-source plugins PureDenoise, StackReg, MicrobeJ (v.5.13l), and ilastik (v.1.3.3post2); and custom code available on the Holden lab Github page: https://github.com/HoldenLab/Ring_Analysis_IJ. Further in vivo data analysis was done using Matlab with custom code available on the Holden lab Github page:

- <https://github.com/HoldenLab/ring-fitting2>
- <https://github.com/HoldenLab/violinplusDABEST-Matlab>
- <https://github.com/HoldenLab/ring-simulator>

For manuscripts utilizing custom algorithms or software that are central to the research but not yet described in published literature, software must be made available to editors and reviewers. We strongly encourage code deposition in a community repository (e.g. GitHub). See the Nature Portfolio [guidelines for submitting code & software](#) for further information.

Data

Policy information about [availability of data](#)

All manuscripts must include a [data availability statement](#). This statement should provide the following information, where applicable:

- Accession codes, unique identifiers, or web links for publicly available datasets
- A description of any restrictions on data availability
- For clinical datasets or third party data, please ensure that the statement adheres to our [policy](#)

All the necessary codes to replicate and analyse the simulation data presented in this work is available for download at the following UCL public data repository: <https://doi.org/10.5522/04/24754527> -- Note that this repository will only be activated upon publication of the work, if you need to access it before we can provide a private link via email.

Live cell imaging of FtsZ rings data presented in this work is from Whitley, K. et al., Nat. Comms. 2021 (doi: 10.1038/s41467-021-22526-0).

High-Speed Atomic Force Microscopy data presented in this work is from Dunajova, Z. et al., Nat. Phys. 2023 (doi: 10.1038/s41567-023-02218-w).

TIRF microscopy data presented in this work is from:

1. Baranova, N. and Loose, M., Methods in Cell Biology, Academic Press 2017 (doi: 10.1016/bs.mcb.2016.03.036)
2. Caldas, P. et al., Methods in Cell Biology, Academic Press 2020 (doi: 10.1016/bs.mcb.2020.01.006)
3. Baranova, N. et al., Nat. Microbio. 2020 (doi: 10.1038/s41564-019-0657-5)

Human research participants

Policy information about [studies involving human research participants and Sex and Gender in Research](#).

Reporting on sex and gender

Population characteristics

Recruitment

Ethics oversight

Note that full information on the approval of the study protocol must also be provided in the manuscript.

Field-specific reporting

Please select the one below that is the best fit for your research. If you are not sure, read the appropriate sections before making your selection.

Life sciences Behavioural & social sciences Ecological, evolutionary & environmental sciences

For a reference copy of the document with all sections, see [nature.com/documents/nr-reporting-summary-flat.pdf](https://www.nature.com/documents/nr-reporting-summary-flat.pdf)

Life sciences study design

All studies must disclose on these points even when the disclosure is negative.

Sample size	<p>Simulation data: Replica numbers were chosen to guarantee sufficient sampling of stochastic processes and were limited by computational cost.</p> <p>In vitro data: Sample sizes were not chosen according to a statistical test, but were limited by practicality and throughput</p> <p>In vivo data: No a priori sample size calculations were performed. No specific sample size was chosen as the single cell / single molecule nature of the measurements means moderate to large sample size, sufficient for robust statistical analysis, is usually straightforward to achieve.</p> <p>In general, numbers of data points, simulation replicas and experimental counts are always specified in figure captions appropriately.</p>
Data exclusions	<p>Simulation data: No data was excluded from analysis.</p> <p>In vitro data: Images were only excluded when supported lipid bilayers were defective.</p> <p>In vivo data: In total 42 Z-rings (6%) were manually excluded due to failure of the joint septal localisation and background subtraction algorithm.</p>
Replication	<p>Simulation data: simulations were run several times (see sample size numbers in manuscript) for each condition described, each with a</p>

Replication	different random number generator seed to guarantee proper sampling of the stochastic processes simulated. In vitro data: The results were verified and reproduced with different batches of purified FtsZ and FtsA proteins. 5 different experiments were analysed in this work. In vivo data: Z-ring imaging experiments were repeated 3 times using independently-prepared samples.
Randomization	Allocating experimental groups was not relevant for this study as only the Z-ring data involves living organisms and in this case all bacterial cells of a particular strain are genetic clones.
Blinding	Blinding was neither possible nor necessary for this study as only the Z-ring data involves living organisms and in this case 1) all bacterial cells of a particular strain are genetic clones and 2) analyses were not sufficiently subjective to require researcher blinding.

Reporting for specific materials, systems and methods

We require information from authors about some types of materials, experimental systems and methods used in many studies. Here, indicate whether each material, system or method listed is relevant to your study. If you are not sure if a list item applies to your research, read the appropriate section before selecting a response.

Materials & experimental systems

n/a	Involvement in the study
<input checked="" type="checkbox"/>	<input type="checkbox"/> Antibodies
<input checked="" type="checkbox"/>	<input type="checkbox"/> Eukaryotic cell lines
<input checked="" type="checkbox"/>	<input type="checkbox"/> Palaeontology and archaeology
<input checked="" type="checkbox"/>	<input type="checkbox"/> Animals and other organisms
<input checked="" type="checkbox"/>	<input type="checkbox"/> Clinical data
<input checked="" type="checkbox"/>	<input type="checkbox"/> Dual use research of concern

Methods

n/a	Involvement in the study
<input checked="" type="checkbox"/>	<input type="checkbox"/> ChIP-seq
<input checked="" type="checkbox"/>	<input type="checkbox"/> Flow cytometry
<input checked="" type="checkbox"/>	<input type="checkbox"/> MRI-based neuroimaging